Study of energy conversion and partitioning in the magnetic reconnection layer of a laboratory plasma[a)]

Masaaki Yamada,[1,b)] Jongsoo Yoo,[1] Jonathan Jara-Almonte,[1] William Daughton,[2] Hantao Ji,[1] Russell M. Kulsrud,[1] and Clayton E. Myers[1]
[1]*Princeton Plasma Physics Laboratory, Princeton University, Princeton, New Jersey 08543, USA*
[2]*Los Alamos National Laboratory, Los Alamos, New Mexico 87545, USA*

(Received 17 December 2014; accepted 6 March 2015; published online 15 May 2015)

While the most important feature of magnetic reconnection is that it energizes plasma particles by converting magnetic energy to particle energy, the exact mechanisms by which this happens are yet to be determined despite a long history of reconnection research. Recently, we have reported our results on the energy conversion and partitioning in a laboratory reconnection layer in a short communication [Yamada *et al.*, Nat. Commun. **5**, 4474 (2014)]. The present paper is a detailed elaboration of this report together with an additional dataset with different boundary sizes. Our experimental study of the reconnection layer is carried out in the two-fluid physics regime where ions and electrons move quite differently. We have observed that the conversion of magnetic energy occurs across a region significantly larger than the narrow electron diffusion region. A saddle shaped electrostatic potential profile exists in the reconnection plane, and ions are accelerated by the resulting electric field at the separatrices. These accelerated ions are then thermalized by re-magnetization in the downstream region. A quantitative inventory of the converted energy is presented in a reconnection layer with a well-defined, variable boundary. We have also carried out a systematic study of the effects of boundary conditions on the energy inventory. This study concludes that about 50% of the inflowing magnetic energy is converted to particle energy, 2/3 of which is ultimately transferred to ions and 1/3 to electrons. Assisted by another set of magnetic reconnection experiment data and numerical simulations with different sizes of monitoring box, it is also observed that the observed features of energy conversion and partitioning do not depend on the size of monitoring boundary across the range of sizes tested from 1.5 to 4 ion skin depths. [http://dx.doi.org/10.1063/1.4920960]

I. INTRODUCTION

Magnetic reconnection is the process by which magnetic field lines in plasmas change topology, liberating magnetic energy to heat the plasma, and accelerate particles to very high energies. It is one of the most fundamental plasma processes at work in laboratory, space, and astrophysical plasmas. It is the underlying mechanism for sawtooth crashes in tokamaks, for geomagnetic substorms in the Earth's magnetosphere, and for solar flares. It is also widely believed to play an important role in energy dissipation processes powering high-energy flaring emission in numerous astrophysical systems. Examples include the magnetospheres of pulsars, magnetars, and accreting black holes; pulsar winds and pulsar wind nebulae; hot, magnetically active coronae of stars and of accretion disks around young stellar objects, neutron stars, and black holes; and in relativistic jets in Active Galactic Nuclei (AGN) and Gamma Ray Bursts (GRBs).[1–6] Research on magnetic reconnection, which started with observations of the solar corona and in the earth's magnetosphere, was dominated by theory in the early phase. Recent progress in understanding the physics of magnetic reconnection has been made through the coordination of results from all three fronts of research: space and astrophysical observations, laboratory experiments, and theory and numerical simulations.[1–3]

The most important feature of magnetic reconnection is that significant acceleration and heating of plasma particles occurs at the expense of magnetic energy. An example of this efficient energy conversion is the observation of large amounts of high energy electrons associated with the reconnection of magnetic field lines in solar flares.[7] In the reconnection region of the Earth's magnetosphere and solar wind,[8,9] convective outflows have been documented by *in-situ* satellite measurements, but the exact physical mechanisms for bulk plasma heating and particle acceleration and energy flow channels remain unresolved. This paper addresses this unresolved key question: how is magnetic energy converted to plasma kinetic energy? Furthermore, the conversion of magnetic energy and its partitioning are quantitatively studied in a laboratory reconnection layer by assessing the overall energy inventory and partitioning in a well defined boundary.

In the classical Sweet-Parker model, based on resistive magneto-hydrodynamics (MHD), the energy dissipation rate is small ($\sim(B^2/2\mu_0)V_AL/S^{1/2}$) due to the slow reconnection rate; $S \gg 1$ is the Lundquist number.[3,10,11] At the same time, it is important to note that the outgoing magnetic flux energy through the thin diffusion region is much smaller than the incoming magnetic energy in this model shown in Fig. 1. Almost all of the incoming magnetic energy is expected to be converted to particle energy within the narrow diffusion

[a)]Paper BI2 5, Bull. Am. Phys. Soc. **59**, 26 (2014).
[b)]Invited speaker.

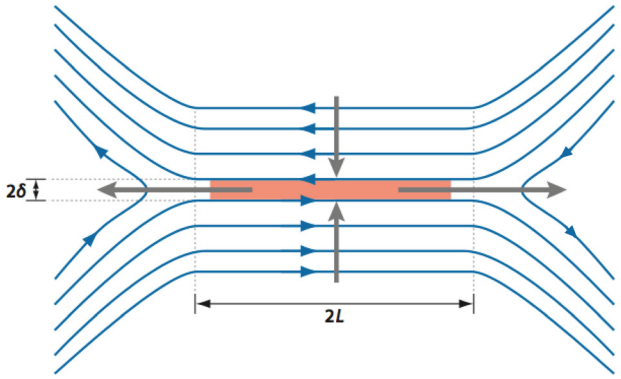

FIG. 1. Magnetic field geometry for the Sweet-Parker model. Oppositely directed field lines are brought together and reconnect in a diffusion layer (red color). The plasma is heated by Ohmic dissipation at the diffusion region and accelerated by the pressure gradient and the tension force. The field line diffuses over the half width of the diffusion layer, δ, which is much smaller than the system size, L.

region. The plasma is heated (slowly) by classical resistive dissipation (ηJ^2) in the diffusion region and is accelerated to the Alfvén velocity due to both the pressure gradient and magnetic tension forces. In the exhaust, there is an equal partition between the flow and enthalpy energy increase, $\Delta(5nk_BT/2) \sim nmv_{out}^2/2$, indicating that magnetic reconnection generates Alfvénic flows of heated plasma at the end of the very narrow exhaust.[11] Recent space observations and numerical simulations show, however, that these predictions are not verified during collisionless reconnection.[12–14] A main reason for it is now considered due to two-fluid physics dominant in the reconnection layer.

In the collisionless magnetic reconnection layer, electrons and ions move quite differently due to two-fluid dynamics;[1,3,15,16] differential motion between the strongly magnetized electrons and the unmagnetized ions generates strong Hall currents in the reconnection plane as shown in Fig. 2. As magnetic reconnection is induced with oppositely directed field lines being driven toward the X point ($\mathbf{B} = 0$ at the center of the layer), ions and electrons also flow into the reconnection layer. The ions become demagnetized at a distance of the ion skin depth ($d_i = c/\omega_{pi}$, where ω_{pi} is the ion plasma frequency) from the X point where they enter the so-called ion diffusion region, and they change their trajectories and are diverted into the reconnection exhaust as seen Fig. 2. The electrons, on the other hand, remain magnetized through the ion diffusion region and continue to flow toward the X point. They become demagnetized only when they reach the much narrower electron diffusion region as seen in Fig. 2. In the MRX experiment, this two-scale diffusion layer was identified with the electron diffusion region residing inside the ion diffusion region.[3] In this situation we define the ion diffusion region as the regime of $\mathrm{E} + \mathrm{Ui} \times \mathrm{B} \neq 0$ and the electron diffusion region as the regime of $\mathrm{E} + \mathrm{Ue} \times \mathrm{B} \neq 0$. In this two-fluid model, the expanding exhaust region becomes triangular in shape and the outgoing magnetic flux through this region is expected to be sizable, while the incoming magnetic energy is quickly converted to particle energy in this X-shaped reconnection layer.

In the two-fluid formulation, the resistive Ohm's law of MHD should be replaced by the generalized Ohm's law in order to describe force balance of an electron flow, namely,

$$\mathbf{E} = \eta\mathbf{J} + \frac{\mathbf{J_e} \times \mathbf{B} - \nabla \cdot \mathbf{P_e}}{en_e} - \frac{m_e}{e}\frac{d\mathbf{V_e}}{dt}. \quad (1)$$

Here, the conventional notations are used together with electron flow velocity, $\mathbf{V_e}$, and spatially dependent electron pressure tensor, $\mathbf{P_e}$.[3] A large out-of-plane electric field caused by the Hall currents in the reconnection layer ($\mathbf{J}_{Hall} \times \mathbf{B}$) causes an increase in the reconnection rate[3,17] by inducing rapid movement of the reconnecting field lines. This explains why the reconnection rate in collisionless plasmas is much faster than the classical Sweet-Parker rate. In addition, a sizable outgoing magnetic flux is expected to be present, since the exhaust region of the reconnection layer contains a large amount of outgoing Poynting vector and is not restricted to be in a thin current sheet of the Sweet-Parker model. Recently, a saddle-shaped strong potential well profile was measured in the MRX (Magnetic Reconnection Experiment) reconnection layer, and found to play a key role in accelerating and heating ions.[18] This observation is consistent with the physics of reconnection in the magnetosphere, where two-fluid effects are dominant.[9]

In the laboratory, ion heating in plasma during reconnection has been observed in a wide range of magnetic configurations such as the reversed field pinch (RFP)[19–21] and spheromaks.[22,23] Local heating in the reconnection layer of dedicated reconnection experiments has been also observed for both ions[24,25] and electrons.[26,27] However, the detailed physics mechanisms behind the observed heating are not well understood.

In spite of recent progress, a major question remains unresolved: How do field lines break and how is energy converted from the magnetic field to plasma particles? A simple 2D numerical simulation (without an out-of-plane guide field) would predict that energy dissipation (due to $\mathbf{J} \cdot \mathbf{E}$) is

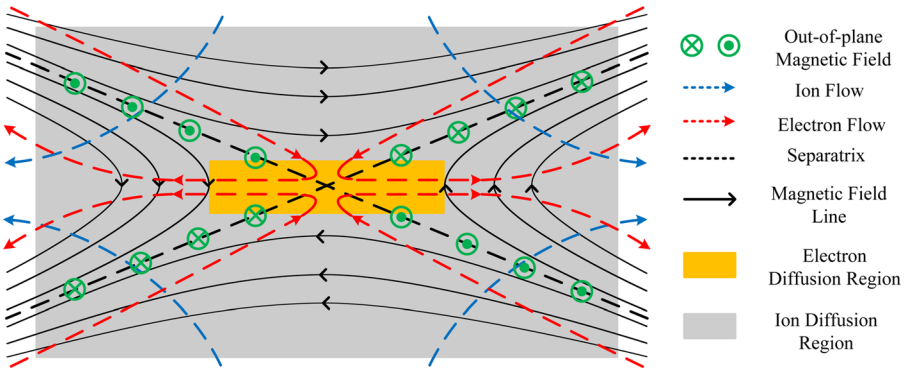

FIG. 2. Schematic diagram of two fluid dynamics in the reconnection layer. Electrons and ions move quite differently generating out-of-plane quadrupolar field (green). Flow of electrons (red broken lines) and ions (blue) in the reconnection plane together with reconnecting field line components projected in the reconnection plane.

localized in the small electron diffusion region, whose width is on the order of the electron skin depth (c/ω_{pe}).[28–31] However, electron heating is observed in a much wider region with the width of 10–20 c/ω_{pe}. It is suggested that the anomalous electron heating takes place near the electron diffusion region and that the high heat conduction should produce heated electrons in the exhaust direction.[27,32] Understanding how electrons gain energy from reconnection in collisionless regimes is of central importance in the present research of magnetic reconnection.

Comparisons among various 2D fluid and kinetic simulations of the current sheets have shown that the final states are often surprisingly similar[33–35] suggesting that the precise dissipation mechanism does not strongly affect the total amount of energy released when the diffusion region is well localized. However, the precise partition of this energy into ion and electron heating has not been studied well. Within collisionless regimes, the electron heating is highly anisotropic which can feedback on the structure of the diffusion region;[36] however, these effects are suppressed in semi-collisional two-fluid regimes.[37] Recent kinetic simulations have empirically shown[38] that the electron heating scales with upstream Alfvén speed, in a similar manner to spacecraft observations.[39] However, the physics behind this scaling for electron heating is not well understood.

Observations in space and laboratory plasmas suggest that a significant fraction of the energy released during reconnection is converted to ion thermal energy[13,32] in the reconnection layer. Recently, a more quantitative analysis of the energy conversion rate has been carried out together with more accurate identification of energy flow processes.[32] The energy partition measured in the magnetotail is notably consistent with the recently obtained MRX data. More than 50% of the magnetic energy flux is converted to the particle energy flux with a high speed ($0.1V_A$) and then branched off to the ion and electron enthalpy fluxes with 2 to 1 ratio. This paper describes this recent experimental investigation more in detail based on accurately measured data from a prototypical laboratory reconnection layer generated in MRX. In addition, a systematic simulation study using a PIC code[40] is carried out to investigate how the branching ratio of energy flows to ions and electrons depends on the boundary condition and the size of monitoring boundary box. The energy inventory in simulations with two types of the global boundary conditions (the MRX boundary condition[41] and the open boundary condition[42]) is qualitatively similar to that of the MRX experiment. We find that the energy inventory is approximately independent of the size of monitoring boundary, as long as it is larger than d_i and smaller than the total system size.

II. EXPERIMENTAL SETUP AND PLASMA PARAMETERS

We have used the MRX facility to experimentally study the conversion of magnetic energy to particle energy in a nearly collision-free reconnection layer. Fig. 3(a) shows a schematic of the MRX apparatus, wherein two oppositely directed field lines merge and reconnect. Experiments are carried out in a setup in which two toroidal plasmas with annular cross section are formed around two flux cores as shown in Fig. 3(a). Each flux core (darkened section in Fig. 3(a)) contains both toroidal field (TF) and poloidal field (PF) coils. After a poloidal magnetic field is created by the PF coil currents, an inductive helium discharge is created around each flux core by pulsing the TF currents in the coils.[43] After the annular plasmas are created, the PF coil current can be increased or decreased in order to drive different modes of reconnection. For decreasing PF current, the poloidal flux in the common plasma is pulled back toward the X point (pull mode); this mode was used for the present experiment.[43] For standard conditions of $n_e = 2$–6×10^{13} cm^3, $T_e = 5$–15 eV, $B = 0.1$–0.3 kG, $S > 400$; the electrons are well magnetized ($\rho_e \ll L$; ρ_e is the electron gyroradius); L is the system size while the ions are not. The mean free path for electron-ion Coulomb collisions is in the range of 5–20 cm (lesser than the layer thickness), and, as a result, the reconnection dynamics are dominated by two fluid and kinetic effects.[1,3] We employ a geometry (R, Y, Z) with B_Z is reconnecting field component and Y being out of plane axis.

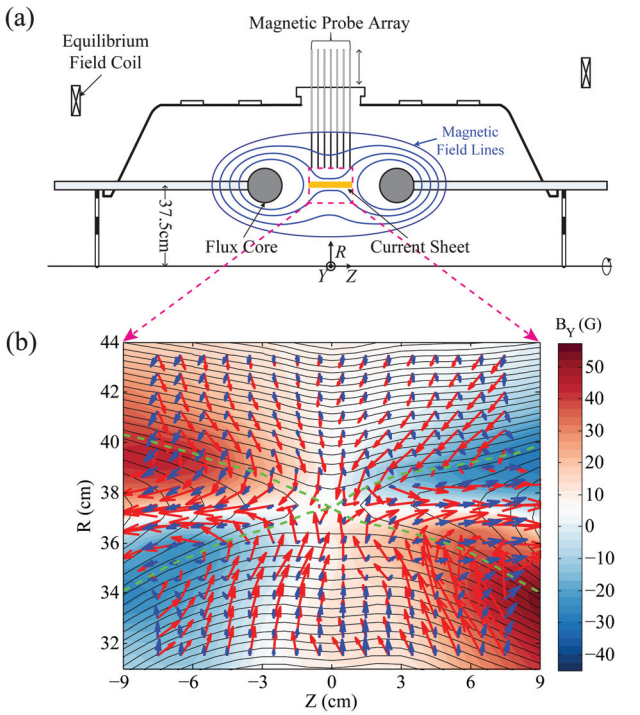

FIG. 3. (a) MRX apparatus and reconnection drive, (b) measured flow vectors (length represent velocity) of electrons (red arrows) and ions (blue) in the full reconnection plane together with poloidal flux contours (which represent reconnecting field line components projected in the reconnection plane) and out of plane field contours; 1 cm vector length stands for 2×10^6 cm/s, color contours represent out-of-plane field strength, and green broken lines depict (experimentally identified) separatrix lines. An azimuthal symmetry is assumed. For standard conditions, $n_e = 2$–6×10^{13} cm^{-3}, $T_e = 5$–15 eV, $B = 0.1$–0.3 kG, $S > 400$ in Helium plasmas.

Figure 3(b) depicts the measured flow vectors of ions (in blue) and electrons (red) in the whole reconnection plane together with poloidal flux contours (representing magnetic field lines) and colored contours of the out-of-plane magnetic field component. There are clear differences between the ion and electron flow patterns, which demonstrates the two-fluid dynamics in the MRX diffusion layer.

Various diagnostics are employed to study the comprehensive dynamics of plasma particles and mechanisms for energy conversion in the reconnection layer. Triple Langmuir

probes are used to measure the electron temperature and density. The density measurements are calibrated by data from a CO_2 interferometer. A radial profile of the floating potential is obtained from a 17-tip floating potential probe with maximum resolution of 7 mm. Local ion temperature is measured by ion dynamics spectroscopy probes (IDSPs),[44] which obtain the spectrum of the He II 4686 Å line, which is subsequently fitted to a sum of 13 Gaussian functions in order to take fine structure effects into account; without considering fine structure, the ion temperature is over-estimated by 15%–25%. The time and spatial resolution of the IDSPs are 5.6 μs and 3–4 cm, respectively. Mach probes are used to measure the ion flow velocity due to its better spatial and temporal resolutions. The data from the Mach probe are calibrated by spectroscopic measurements from the IDSPs. The electron flow vectors in the reconnection plane are derived by electron current profile from the magnetic profile, measured by fine scale magnetic probes; using $\mu_0\mathbf{J} = \nabla \times \mathbf{B}$ and $\mathbf{V}_e = -\mathbf{J}/en_e + \mathbf{V}_i$.

In order to select the final dataset, more than 4200 discharges were scrutinized based on the reproducibility of the data from the 2-D magnetic probe array and a reference Langmuir probe. The main criteria are the location of the X point, the total plasma current, and the density and temperature measured by a reference Langmuir probe. The data values at each measurement point are determined by averaging over 7–15 discharges. The error bars for each measurement are chosen between the standard deviation of each data set and the uncertainty in measurements, whichever is larger. Typical errors in magnetic field measurements are less than 10%, while those in electrostatic measurements are 15%. The uncertainty in the ion temperature measurements mostly comes from the fitting process and is typically about 15%.

III. ELECTRON DYNAMICS AND HEATING IN THE TWO-FLUID RECONNECTION LAYER

A. Electron flow dynamics studied by flow vectors

From measurements of profiles of magnetic field lines, electric field and the local flow vectors of electrons and ions, the dynamics of the plasma particles can be studied in significant detail. As the $\mathbf{E} \times \mathbf{B}$ ($\mathbf{E}$ is the reconnection electric field and $\mathbf{B}$ reconnecting magnetic field) drift motion drives electrons towards the X point together with field lines (Fig. 3(b)), the magnetic field strength weakens. As a result, the electron drift (E/B) velocity in the reconnection plane becomes very large near the X point and electrons are ejected out to the exit. Fig. 4(a) presents more detailed measurements of the electron flows in one half of the reconnection plane. Ions, which become demagnetized as they enter the ion diffusion region whose width is $\sim d_i$ (5–6 cm), are accelerated while moving in the ion diffusion region and flow outward to the exhaust direction (as seen in Fig. 3(b)). In contrast, the magnetized electrons flow inwards towards the X point along field lines, which are almost parallel with the separatrix at the edge of the inflow region. This electron flow pattern generates net circular currents in the reconnection plane, and thus creates an out-of-plane magnetic field with the quadrupole profile as shown in Fig. 3(b), and represented in 3D in Fig. 4(a). This is a signature of the Hall effect and our experimental data show a very good agreement with

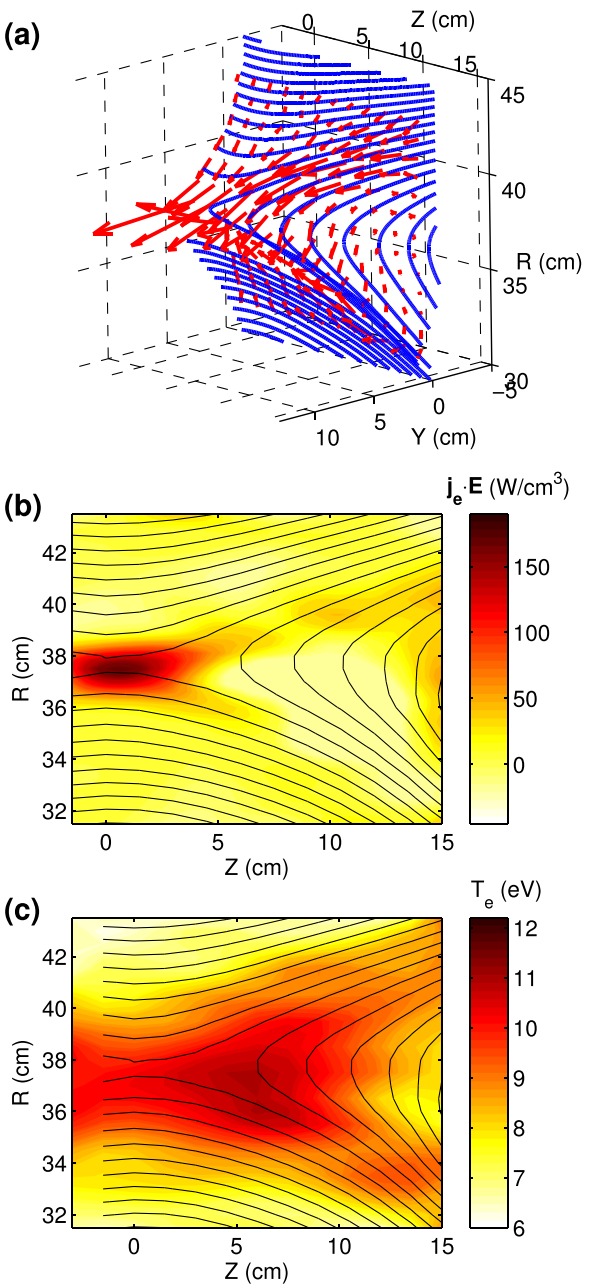

FIG. 4. (a) Measured flow vectors of electrons in a half of the reconnection plane in its bird's eye view (in 3-D geometry). While ions and electrons move together with field lines before entering the ion diffusion region, electrons move much faster as they reach toward the X point region. (b) the energy deposition to electrons, $\mathbf{J_e} \cdot \mathbf{E}$, is concentrated near the X point, (c) Strong electron temperature rise is observed in the wide area of the exhaust region. Strong parallel heat conduction is considered to cause the high T_e at the exhaust region.

typical Particle-in-Cell (PIC) simulations.[28,45,46] The measured amplitude of this Hall quadrupole magnetic field is of the order 40–60 G (Refs. 47 and 48) compared with 100–120 G reconnecting field strength. The increased reconnection electric field, caused by the strong Hall term ($\mathbf{J} \times \mathbf{B}$) and a steady current of electrons, leads to the observed fast motion of flux lines ($E = -d\Psi/dt$) in the reconnection plane, or the fast reconnection rate, as shown in Eq. (1).

As the incoming field lines are stretched toward the Y direction (out of plane), as shown in Fig. 4(a), magnetic field lines break and electrons flow out rapidly to the exhaust

direction. In the upstream (inflow) section of the MRX reconnection layer, a slow electron inflow velocity ($V_e \sim V_i \ll V_A$) is seen while much faster electron flow velocity is measured ($\sim 5V_A$) in the y direction near the X point region as shown in Fig. 4(a). It should be noted that electrons flow out almost orthogonal to magnetic field lines near the X point region. While electrons flow out of the X point region, reconnection of magnetic field lines occurs and electrons pull newly reconnected field lines towards the exhaust in the outflow region. The magnetic field lines in the inflow region move quickly, as reconnection occurs near the X point, while in the exhaust region, they slowly cross the separatrices.

B. Observation of electron heating

The energy deposition rate on electrons, $\mathbf{J_e} \cdot \mathbf{E}$, is concentrated near the X point as seen in Fig. 4(b), in a much wider region ($\sim 10d_e$) than predicted by numerical simulations.[31] Furthermore, our data indicates that electron heating takes place in even wider region of the exhaust as seen in Fig. 4(c). The measured 2-D electron temperature profile shows that the electron heating region expands along the magnetic field lines in the exhaust. We observe electrons are heated in a wide region with the width of $\sim 0.5d_i$. Strong parallel heat conduction is considered to cause the wide observed region of high T_e. Based on 2-D energy transport analysis, we note that Ohmic dissipation based on the perpendicular Spitzer resistivity accounts for less than 20% of the required heating power.[27] Magnetic and electrostatic fluctuations in the lower hybrid frequency range are observed[26,49] near the X point and throughout the downstream region[27] and are believed to cause the observed anomalous electron heating. However, more quantitative analyses on wave-particle interactions are required.

With the limited accuracy of our directional plane probes, some anisotropy is indicated with $T_{eZ} > 1.5T_{eY}$ just outside of the electron diffusion layer. While the magnitude of the magnetic field decreases toward the X point, the total electron kinetic and thermal energy with respect to magnetic energy increases substantially. As the electron beta, $\beta_e = 2\mu_0 n_e T_e / B^2$ is initially 0.1 before reaching the reconnection region, it is well over unity inside the broad electron diffusion region, breaking the condition of a magnetically confined state, as clearly seen in Fig. 4(a). This condition could induce firehose instability in the region, although the error bars of the measurement are too large for an exact stability analysis of the firehose instability.

IV. GENERATION OF AN ELECTRIC POTENTIAL WELL IN THE TWO-FLUID RECONNECTION LAYER

Recently, it has been experimentally verified in MRX that a saddle shaped electric potential profile is formed in the reconnection plane in order to balance the Lorentz force on the electron flows.[18] It is found that the flows of magnetized electrons, which cause the Hall effects, produce a strong electric field in the reconnection plane especially across the separatrices as shown in Figs. 5(a) and 5(b). A strong in-plane electric field is generated near the separatrices with a wider and deeper potential well downstream. The MRX potential data are consistent with recent simulation results[30,31] as well as the measurements by the CLUSTER spacecraft[9] which showed a narrow potential well near the X point with a half width in the range of 60–100 km [(3–5) d_e], and deeper and wider well towards the exhaust region. In the experiment, the electron diffusion region near the X point was observed to be significantly wider than the electron skin depth[46,49] in contrast with 2D numerical simulations.[30,31] The in-plane (Hall) electric field (or potential drop) is mostly perpendicular to the local magnetic field lines and is strongest near the separatrices. Electric potential is seen to be nearly constant along a poloidal flux contour (or magnetic field line)) in a half of the reconnection plane in Fig. 5(a). In this figure, we notice that a large electric field across the separatrices extends to a significantly larger area of the reconnection layer ($L \gg d_i$), than the region in which field line breaking and reconnection occur. A typical magnitude of the in-plane electric field, E_{in} is $\sim$700 V/m, which is much larger than the reconnection electric field, $E_{rec} \sim 200$ V/m.

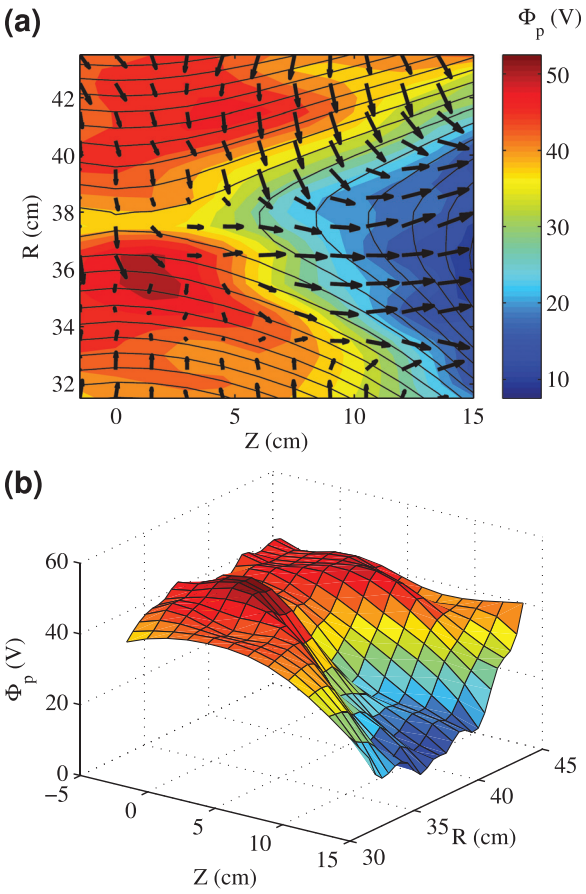

FIG. 5. Potential profile of the two-fluid reconnection layer together with ion flow vectors. The saddle-shape electrostatic potential profile (a) deduced from multiple Langmuir probe measurements and a birds-eye view of the profile. (b) The measured potential profile in MRX is divided into four regions by the separatrix lines shown in Fig. 2 with electric potential tends to be constant along magnetic field lines. (a) Also contains ion flow vectors measured by Mach probes in the reconnection plane.

V. ION ACCELERATION AND HEATING IN THE TWO-FLUID RECONNECTION LAYER

We observe direct acceleration of ions near the separatrices due to the strong electric field mentioned above, whose spatial scale is $\sim$2 cm, smaller than the ion gyro-radius of $\sim$5 cm.

Fig. 5(a) shows 2D profile of ion flow vectors measured by Mach probes, along with poloidal flux contours and contours of electric potential Φ_p. One can notice clearly that ion flows change their directions at the separatrices and are accelerated in both the Z and the R directions. Fig. 6(a) shows profiles of the energy deposition to ions through $\mathbf{J_i} \cdot \mathbf{E}$. It is found that the energy deposition to ions occurs primarily in the exhaust side of separatrix lines. Fig. 6(b) depicts the spectrum of the 4686 Å line of He II ions measured by the IDSP probes at three locations. The He II spectral lines are renormalized by local ion thermal velocity. The spatial resolution of this local spectroscopic measurement is 4 cm. This spectral profile represents the local velocity distributions of ions versus v_Z. Shifted Maxwellian distributions are observed at three typical positions as shown in Fig. 6(b). The corresponding measurement locations in the simulations are marked in Fig. 6(a). A notable heating is observed as the ions flow out to the exhaust from the X region, as demonstrated in Fig. 6(b). The maximum ion outflow of 1.6×10^6 cm/s corresponds to 5 eV of energy per helium ion, which is much smaller than the magnitude of the potential decrease across the separatrices ($\sim$30 V). This indicates that ions must lose considerable momentum as they pass through the downstream region.

The cause of this anomalously fast slowdown of ions, together with ion heating, is considered to be due to "remagnetization" of the outgoing ions. Since it is very difficult to verify this mechanism experimentally, 2-D fully kinetic simulations have been carried out to verify this remagnetization and understand how ions are heated downstream. In these simulations, realistic MRX global boundary conditions are used in the particle-in-cell (PIC) code VPIC.[40] In addition, Coulomb collisions are modeled using the Takizuka-Abe particle-pairing algorithm[42,50] for realistic MRX conditions, such that ν_{ii}/Ω_i and $\lambda_{i,mfp}/d_i$ are matched to the experimentally measured values, where ν_{ii} is the ion-ion collision frequency, Ω_i is the upstream ion cyclotron frequency, and $\lambda_{i,mfp}$ is the ion mean free path. As the normal component of reconnected magnetic field becomes stronger further downstream as shown in Fig. 6(c), the ion trajectory is significantly affected by the magnetic field of the exhaust, and thus ions are remagnetized. With collisions, ions are almost fully thermalized with a higher temperature than the initial value. We note that the ion and electron dynamics are primarily dictated by (collision-free) two-fluid physics even some energy loss mechanisms are influenced by collisions.

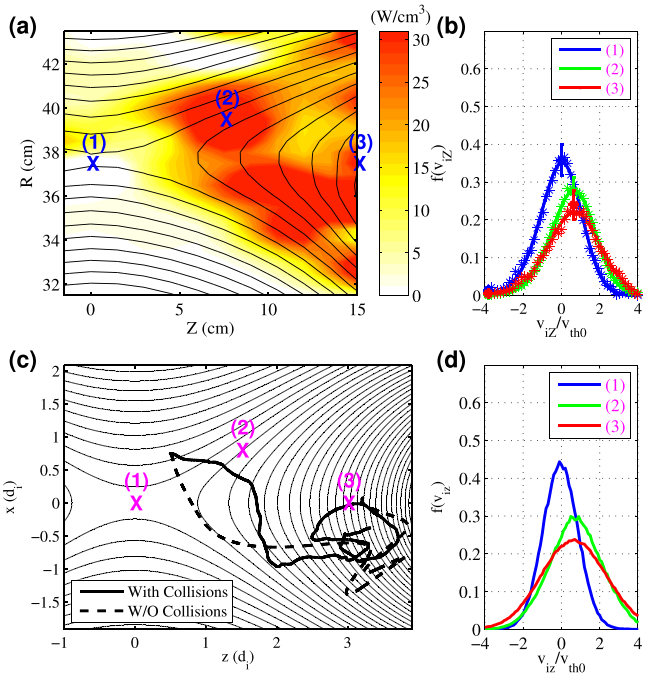

FIG. 6. Ion dynamics in the ion diffusion region and sample distribution functions. (a) 2D profile of measured energy deposition to ions through $\mathbf{J_i} \cdot \mathbf{E}$, along with contours of poloidal flux. Across the separatrices, ions are accelerated toward the exhaust direction. (b) Normalized spectra of measured He II 4686 Å line at three different locations specified with crosses in (a). The He II spectral lines are renormalized by local ion temperature. (c) Sample ion trajectories in a VPIC simulated reconnection plane with (thick solid line) and without (thick dashed line) collisions. (d) Corresponding data from numerical simulation to the measurement (b) is shown.

We obtain a good agreement between the observed ion temperature profile and numerical simulation results only with the correct collision frequencies. Figure 6(d) shows the ion distribution functions in the simulation at three locations; at the X point, separatrix, and exhaust. With realistic collisions, ions are almost fully thermalized at the exhaust with a higher T_i than the upstream value. In the collisionless simulation, on the other hand, the ion distribution is different from Maxwellian, although a broadening in the ion distribution exists when it is compared to that at the X point. These results indicate that ion thermalization is due both to remagnetization and to collisional effects in the downstream region.

VI. TRANSPORT PROCESSES AND ENERGY INVENTORY IN THE TWO-FLUID RECONNECTION LAYER

During the two-fluid reconnection process described above, magnetic energy is converted to the kinetic and thermal energy of both electrons and ions. It is shown that electrons gain energy near the X point mostly from the inductive reconnection electric field and that anomalous electron heating occurs around the electron diffusion region. The high electron temperature spreads quickly along the magnetic field lines in the exhaust region. Ions gain energy mostly from the Hall electric field over the broad downstream region. Now, one important question is how much energy is transported to particles and what the partitioning of this energy is.

Using an equation of energy transport analogous to that adopted by Birn and Hesse,[12] one can evaluate how much of the magnetic energy is converted to the kinetic energy of electrons and ions by assessing the energy inventory of the reconnection layer

$$\frac{\partial}{\partial t}\left[\frac{B^2}{2\mu_0}+\sum_{s=e,i}\left(\frac{3}{2}n_sT_s+\frac{\rho_s}{2}V_s^2\right)\right] +\nabla\cdot\left[\mathbf{S}+\sum_{s=e,i}\left(\frac{5}{2}n_sT_s\mathbf{V_s}+\frac{\rho_s}{2}V_s^2\mathbf{V_s}\right)\right]=\sum_{s=e,i}L_s, \quad (2)$$

where L_s is the loss term for the species s including thermal conduction, radiation, and ion energy loss to neutrals. The

energy inventory is calculated by monitoring the flows of magnetic energy, plasma enthalpy, and bulk flow energy simultaneously while measuring the incoming and outgoing magnetic flux (**S**), enthalpy flux, and bulk flow flux (kinetic energy flux) at a set boundary. The boundary of the volume of the plasma, Γ_b, is given by $31.5 \leq R \leq 43.5$ cm and $0 \leq Z \leq 15$ cm ($\sim 2d_i \times 2d_i$), in which all local key parameters of the plasma are measured within 10%–15% of error bars, assuming symmetry with respect to the major axis of the MRX plasma. It is important to include the components of the Hall magnetic fields in both the incoming and exhaust regions in order to calculate the Poynting fluxes. This is quite different situation from the Sweet-Parker formulation in which outgoing magnetic energy is negligible, and thus all incoming energy is converted. As was done in Birn and Hesse,[12] isotropic pressure is assumed in this calculation, which is justified in our plasma where anisotropy was only observed in a small region near the X point.

A. Calculation of the energy inventory

The energy inventory is calculated by integrating the each term in Eq. (2) over the volume Γ_b. The magnetic energy inflow rate is estimated by

$$W_{S,in} = \int_{\Gamma_b} d^3x \nabla \cdot \mathbf{S}_{in}, \tag{3}$$

where $\mathbf{S}_{in} = (E_Y B_Z/\mu_0)\mathbf{e}_R$ is the incoming Poynting flux associated with the reconnecting magnetic field and reconnection electric field. Here, $\mathbf{e}_R$ is the unit vector along the R direction. The outgoing magnetic energy is obtained by integrating the outgoing Poynting flux at the boundary ($Z = 0$ and $Z = 15$ cm). The outgoing Poynting flux is divided into the MHD component, $\mathbf{S}_{MHD} = -(E_Y B_R/\mu_0)\mathbf{e}_Z$ and the Hall field component, $\mathbf{S}_{Hall} = (E_R B_Y/\mu_0)\mathbf{e}_Z - (E_Z B_Y/\mu_0)\mathbf{e}_R$. For collisionless reconnection, S_{Hall} is not negligible especially near the separatrix where both the Hall (quadrupole) magnetic field and the Hall (bipolar) electric field are strong.

If the system is in a steady state, the time-derivative terms of Eq. (2) become zero. However, during the quasi-steady period of MRX, the plasma quantities are slowly changing, while the reconnection rate is almost steady. For example, due to the decreasing PF current, the vacuum component of the magnetic field is decreasing during the quasi-steady period. Thus, the total magnetic energy in Γ_b is also decreasing, which is not negligible due to the large volume over which the integral is conducted. Therefore, the contribution from the time-derivative terms is all included.

Total energy converted to each species per unit time is separately computed by

$$W_s = \int_{\Gamma_b} d^3x \mathbf{J_s} \cdot \mathbf{E}. \tag{4}$$

To obtain change in a specific form of energy, we grouped associated terms in Eq. (2). The flow energy change of species s is given by

$$\Delta W_{K,s} = \int_{\Gamma_b} d^3x \left[\frac{\partial}{\partial t}\left(\frac{\rho_s}{2}V_s^2\right) + \nabla \cdot \left(\frac{\rho_s}{2}V_s^2 \mathbf{V_s}\right)\right]. \tag{5}$$

The thermal energy change of species s is defined as

$$\Delta W_{H,s} = \int_{\Gamma_b} d^3x \left[\frac{\partial}{\partial t}\left(\frac{3}{2}n_s T_s\right) + \nabla \cdot \left(\frac{5}{2}n_s T_s \mathbf{V_s}\right)\right]. \tag{6}$$

We note that quantities in the inflow region are taken into account, although those quantities are much smaller than the incoming magnetic energy due to low $\beta \sim 0.2$ in the inflow region.

We estimate the energy loss rate of each species by considering the electron and ion heat flux, electron energy loss by impurity radiation, and ion energy loss to neutrals by charge-exchange collisions. For the heat flux estimation, the results in Braginskii[51] are used. The impurity radiations are dominated by oxygen radiation, based on spectral measurements of IDSPs. The oxygen radiation is a strong function of T_e and only strong in the downstream region. With 5% of the average concentration, it is estimated to be about 13% of the total electron energy gain, W_e. Due to lack of the neutral density measurement, we assume a flat neutral density profile over the volume Γ_b with the initial neutral density. Because the ionization rate is expected to be over 30% during discharge, this assumption leads to an upper bound ($\sim$0.15 MW) for the ion energy loss to neutrals. The measured neutral temperature profiles show that neutrals are heated during discharge up to 4 eV, which supports the existence of ion energy loss via charge exchange collisions with neutrals.

In Fig. 7, all quantities are shown as rate of energy flow in and out ($W_{M,in} = 1.9$ MW). The outgoing Poynting flux is sizable in MRX where two-fluid reconnection occurs, because the outgoing energy associated with Hall magnetic fields plays a significant role. We have quantitatively evaluated how magnetic energy is converted to the thermal and flow (kinetic) energy of electrons and ions within a cylindrical boundary of radius 12 cm and height 15 cm. In our local energy flux inventory, about a half of incoming magnetic energy is converted to particle energy, 1/3 of which goes to electrons and 2/3 to ions. Our quantitative measurements show that a half of the incoming magnetic energy is converted to particle energy with a remarkably fast speed, ~ 0.1–$0.2(B^2/2\mu_0)V_A$ in comparison with the rate calculated by MHD, $\sim (B^2/2\mu_0)V_A L/S^{1/2} = 0.03(B^2/2\mu_0)$; $S = 900$.

VII. COMPARISON WITH PARTICLE IN CELL (PIC) SIMULATIONS

The results from MRX on energy partitioning have a remarkable resemblance with the recent measurement in the magnetotail of similar size in terms of the ion skin depth ($L \sim 2000$ km $\sim 3d_i$). In the Earth's magnetotail, the energy partition was carefully measured by using Cluster satellite data.[13] The observed energy partition is very similar, namely, 50% of magnetic energy flux being converted to the particle energy flux which is dominated by the ion enthalpy flux, with smaller contributions from both the electron enthalpy and heat flux. This similarity raises the question, of whether there is any fundamental principle underlying these results? To search for reasons, we have carried out 2D PIC simulations with two different boundary conditions.

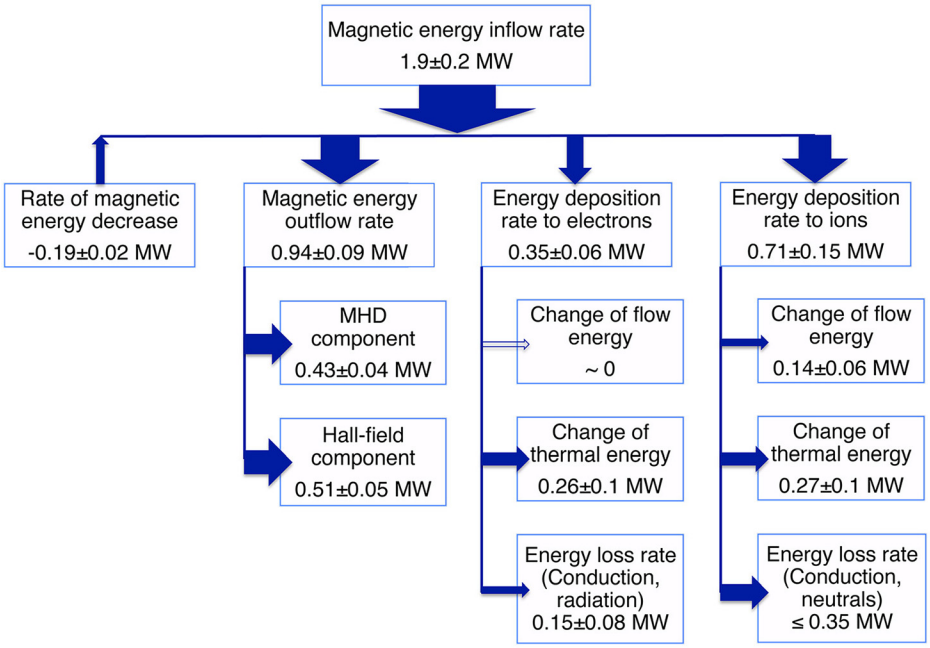

FIG. 7. Energy flow chart in the MRX reconnection layer. The outgoing Poynting flux is sizable in MRX where two-fluid reconnection occurs because of outgoing energy associated with the Hall field components. Our quantitative measurements show that a half of the incoming magnetic energy is converted to particle energy with a remarkably fast speed, $\sim 0.2(B^2/2\mu_0)V_A$. Reprinted with permission from Yamada *et al.*, Nat. Commun. **5**, 4474 (2014). Copyright 2014 Nature Publishing Group.

An additional motivation for comparison with numerical simulations is that there are several possible constraints on the applicability of experimental results to astrophysical and space plasmas, including the effects of different boundary conditions, system size, smaller ion to electron temperature ratio than are found in typical space plasmas (e.g., the Earth's magnetotail). In order to study these constraints, we have analyzed data from fully kinetic simulations, wherein each of these constraints can be independently relaxed. For these purposes, two sets of 2D simulations with different boundary conditions were performed, one with the global MRX boundary conditions described in detail by Dorfman *et al.*,[41] and the other using a standard Harris sheet initial condition and open boundary conditions along the outflow.[42] The geometry of simulation is shown in Fig. 8(a).

For all cases, we have employed the particle in cell code VPIC.[40] Length scales are normalized to the ion skin-depth and time scales are normalized to the upstream ion cyclotron frequency, Ω_i. In the Harris equilibrium, the initial magnetic field profile is given by $\mathbf{B} = B_0 \tanh(x/\delta)\hat{z}$, and the initial density profile is then $n_e = n_b + n_0 \,\mathrm{sech}^2(x/\delta)$. In contrast, the MRX simulation case has an initial field determined by the flux core coil currents, and the initial density profile is uniform.

The Harris sheet simulation case discussed here has been previously reported,[52] although for completeness the simulation parameters are summarized here. The initial sheet thickness is given by $\delta = 0.5d_{i0}$, where d_{i0} is the initial ion skin depth evaluated with n_0. The ion to electron mass ratio is matched to Hydrogen, $m_i/m_e = 1836$, and the sheet temperature ratio is matched to a typical value in the magnetotail, $T_{i0}/T_{e0} = 5$. The background population has a lower electron temperature, $T_{eb}/T_{e0} = 0.76$, giving an upstream temperature ratio of $T_{ib}/T_{eb} \approx 6.6$. The upstream density is $n_b = 0.23n_0$. Due to computational constraints $\omega_{pe}/\Omega_e = 2$ and the domain is $20d_{i0} \times 20d_{i0}$ with open boundaries,[42] and

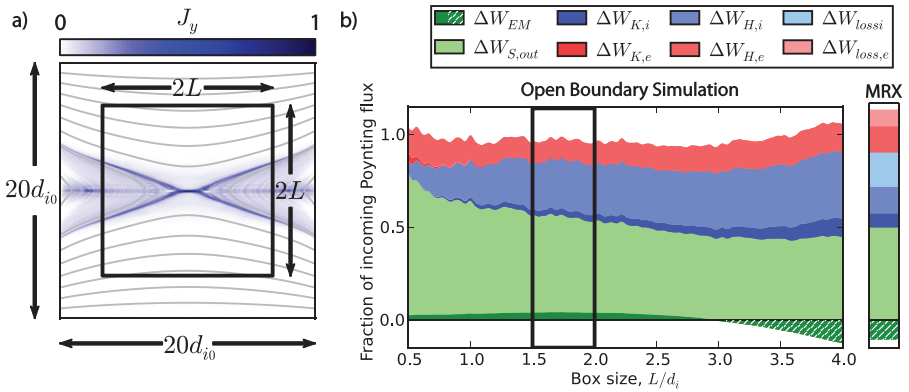

FIG. 8. In the simulations, the energy inventory is computed within a square box of half-length L shown in (a). Note that here we have normalized the box size L to the upstream ion skin depth d_i rather than the initial ion skin depth d_{i0}. For this simulation, $d_i \sim 2d_{i0}$. Remarkably, the energy inventory in the open-boundary simulation (b), is very similar to that in the experiment (right bar), suggesting that downstream boundary conditions do not play a strong role in determining the total energy conversion rate. The dark green hatched regions denote scales where magnetic energy is being depleted rather than stored, and so the total sum of all other terms may exceed 1. In the simulations, the terms do not balance perfectly since the heat flux is not included. In the experiments, heat flux is included in the loss terms $\Delta W_{loss,s}$ along with radiative losses and energy transfer to neutrals.

consists of 5120×5120 cells with $\sim 10^{10}$ particles per species. The MRX simulation was reported initially in Yoo *et al.*[27] and discussed briefly in Sec. V. The size of the boundary box where all relevant energy fluxes are computed is $2d_i \times 2d_i$, where d_i is the ion skin depth evaluated with the upstream density as defined in MRX.

Effects of the boundary conditions on the overall energy inventory can be studied by comparing the two sets of simulations described above. The open boundaries allow continual quasi-steady reconnection to proceed while eliminating any possible effects from downstream boundary conditions, such as the flux cores in both the experiment and MRX simulation, whereas the higher ion to electron temperature ratio and lack of collisions more closely matches space plasmas.

In all cases, the energy inventory is quantitatively evaluated following the same procedure as for the experimental data; however, we neither directly compute nor estimate the heat flux in the simulations. In the experimental results, the heat flux is estimated and incorporated along with estimates for radiation and energy transfer to neutrals into the total loss terms, $\Delta W_{s,loss}$. As shown in Figure 8, the obtained energy inventory in the simulation balances quite well (the sum is approximately 1) despite the neglect of the heat flux terms. As a result, we can conclude that heat flux plays a negligible role in the overall energy balance.

Since we are interested in studying the energy inventory during quasi-steady reconnection, the time window over which we compute the energy inventory is carefully chosen. For the MRX case, we choose data from around the time $t \sim 0.5\tau$, where τ is the flux core driving timescale;[41] while in the Harris sheet case we choose the last time-point of the simulation, $t/\Omega_I = 34$. These choices eliminate any transient phenomena associated with the onset of reconnection and allow for a well developed reconnection layer to be present.

Results from the simulations with the MRX boundary conditions have been reported in Yamada *et al.*[32] and presented in Table I. With a box size of $2d_i \times 2d_i$, the energy inventory of the MRX simulation is qualitatively similar to that of the present experiment. The total outgoing magnetic energy is about 60% of the incoming magnetic energy ($W_{S,in}$). The contribution of the first term on the left-hand-side of Eq. (2) is about 5% of $W_{S,in}$. The energy deposition to electrons (W_e) is about 19% of $W_{S,in}$, and the energy deposition to ions (W_i) is 26% of $W_{S,in}$.

Our results on the energy inventory in the open boundary simulation are shown in Fig. 8. Remarkably, we find that over a broad range of scales, $1.5d_i < L \lesssim 4d_i$, the energy inventory is approximately independent of box size. Furthermore, our simulation results show decent agreement with the experimental results; approximately half of the incoming Poynting flux is converted into particle energy, with most of this energy going to the ion enthalpy. As a result, we can conclude that the experimental constraints outlined above are likely not important in determining the energy conversion efficiency during anti-parallel magnetic reconnection.

VIII. SUMMARY AND DISCUSSIONS

We have observed that the conversion of magnetic energy occurs across significantly larger regions than the narrow electron diffusion region that was considered before for collisionless reconnection. A saddle shaped electrostatic electric potential profile is experimentally verified in the reconnection plane and ions are accelerated by the electric field at the separatrices and heated by remagnetization by the reconnected field lines. Our quantitative measurements of the acceleration and heating of both electrons and ions demonstrate that a half of the incoming magnetic energy is converted to particle energy with a remarkably fast speed.

When a reconnection electric field is applied in a broad region ($\gg d_i$) in which opposite magnetic field lines meet, such as shown in Fig. 3, electrons with high mobility respond to this field by creating a deformed region of magnetic configuration with magnetic and electric fields associated with Hall effects. This separates inflowing field lines from the reconnected ones by separatrices, across which a notable potential drop (strong electric field) occurs. While electrons are heated at the center of reconnection layer, a strong in-plane electric field is generated near the separatrices with a wider and deeper potential well downstream. Ions are accelerated across the separatrices by the strong electric field of the reconnection layer and heated through remagnetization by the magnetic field. This potential structure extends to a very broad region, much wider than the ion skin depth. In our study of a typical reconnection layer in MRX, about a half of the incoming magnetic energy is converted to particle energy, of which 1/3 goes to electrons and 2/3 to ions. The extent of the region where electrons are heated is much wider than the electron diffusion region predicted by 2-D simulations, and ion acceleration and heating occur on significantly larger scales than the ion skin depth.

Recently, in a reconnection region of similar size ($L \sim 2000$ km $\sim 3d_i$) in the Earth's magnetotail, the energy partition was carefully measured by using Cluster satellite

TABLE I. Summary of energy conversion during collisionless reconnection. The quantities are normalized to the magnetic energy inflow rate.

	MRX measurement		Simulation		
	$1.5d_i \times 1.5d_i$	$2d_i \times 2d_i$	MRX boundary	Open boundary	Space observation
Magnetic energy inflow	1.0	1.0	1.0	1.0	1.0[a]
Magnetic energy outflow	0.51	0.49	0.6	0.53	0.1–0.3
Energy deposition to ions	0.31	0.37	0.26	0.29	0.39
Energy deposition to electrons	0.21	0.18	0.19	0.11	0.18

[a]The space data have uncertainties in measurements of the total incoming magnetic energy and the exact size of the boundaries. The energy inventory in MRX is analyzed for a box size of $1.5d_i \times 1.5d_i$ and $2d_i \times 2d_i$. The box size for the simulations is $2d_i$.

data.[13] The observed energy partition is remarkably consistent with the present MRX data, namely, 50% of magnetic energy flux being converted to the particle energy flux which is dominated by the ion enthalpy flux, with smaller contributions from both the electron enthalpy and heat flux.

We compare our data with that of the findings in the magnetotail reconnection layer of similar size ($L \sim 2000$ km $\sim 3d_i$)[13] and find a good agreement as shown in Table I. The numbers from numerical simulations described above are also qualitatively agreed with our measurements. Although it was difficult to determine the exact boundary by their multi-spacecraft timing analysis with the motion of the X-line, the half length of the tail reconnection layer was estimated to be 2000–4000 km, which represents 3–6 ion skin depths (d_i). The normalized scale length of this measurement is thus very similar to our cases, $L \sim 3d_i$. In both measurements, significantly more energy flows to ions than to electrons with non-negligible amount of magnetic energy flowing out the exhaust.

To study reasons for the remarkable similarity between the MRX results and the magnetotail data, we have carried out 2D PIC simulations with two different boundary conditions, one with the global MRX boundary conditions and the other using a standard Harris sheet initial condition with open boundary conditions of variable box size. Surprisingly, we find that over a broad range of scales, $1.5d_i < L \lesssim 4d_i$ (the total system size is 5 d_i), the energy inventory is almost independent of the box size. Furthermore, our simulation results show decent quantitative agreement with the experimental results; approximately half of the incoming Poynting flux is converted into particle energy, with more than a half of this energy going to the ion enthalpy.

As summarized in Table I, the energy inventory in MRX is analyzed for a box size of $1.5d_i \times 1.5d_i$ and $2d_i \times 2d_i$, while the boundary of measuring the energy partitioning constrained by the present MRX geometry to less than $2d_i$. The energy deposition to ions slightly increases over that to electrons as the box size becomes larger, but overall inventory is similar. This trend agrees with results from the open-boundary simulation as highlighted with a black box in Fig. 8(b). As a result, we conclude that MRX experimental conditions are not major constraints regarding energy conversion efficiency and partitioning in the reconnection layer. The major reason for the agreement seems to come from the fundamental local two-fluid reconnection mechanism in which electron's motion near the X-line generates a unique saddle shape potential field with a strong in-plane electrostatic field across the separatrices. This electric field extends beyond multiple skin depth leading to substantial ion energy gain. More quantitative study is needed to find a comprehensive reason behind the observed partitioning of the energy flow.

While kinetic simulations shown in Fig. 8 were performed with a realistic mass ratio for hydrogen ($m_i/m_e = 1836$) and a temperature ratio ($T_i/T_e = 5$) relevant to the magnetosphere, the general applicability of these results is not yet determined. If the system size becomes larger, it will invariably lead even with 2D geometry, to many secondary magnetic islands in both two-fluid and kinetic regimes.[5,53] This may alter the partition of energy, but also makes it more difficult to precisely measure the various terms. In addition, for large 3D systems, this physics leads to the formation and interaction of magnetic flux ropes within the layer[54] leading to the development of turbulence.[55] The influence of these effects on the reconnection rate, particle acceleration and the partition of released energy remain some of the most challenging problems remaining in reconnection physics.

We believe that our study is a first step towards finding a common trend of energy partitioning and particle energization during reconnection. Our comparative study has implications for its scaling with Lundquist number. When we compare our results from plasmas of $S < 1000$ with that of the magnetosphere where the Lundquist number is very large ($>10^8$), we find that the energy flow pattern is very similar, i.e., the energization characteristics do not strongly depend on the Lundquist number. This is consistent with the characteristics of the two-fluid plasma physics where the classical resistivity based on electron-ion collisions does not play a major role.

Finally, in the reversed field pinch (RFP) fusion plasmas where magnetic reconnection plays a key role in self-organized plasma formation and sustainment, it has been reported that a similar portion of magnetic energy (25%–35%) is converted to ion thermal energy.[21] Is there a common physics principle to explain these observations from driven reconnection layers, despite some differences in the boundary conditions? Although it should be noted that the reconnection phenomena occur in the broad region of RFP, the present results may represent a key to our important question, how magnetic energy is transferred to plasma particles in a broad reconnection region.

ACKNOWLEDGMENTS

We thank Dr. S. Zweben for valuable physics discussions and Mr. R. Cutler for technical supports. This work was supported by DOE Contract No. DE-AC0209CH11466 and NASA program for the MMS mission under Grant No. NNH11AQ45I. Contributions from W. Daughton were supported by NASA's Heliophysics Theory Program, and simulations were performed with resources from the LANL Institutional Computing Program.

[1]M. Yamada, Phys. Plasmas **14**, 058102 (2007).
[2]E. G. Zweibel and M. Yamada, Annu. Rev. Astron. Astrophys. **47**, 291 (2009).
[3]M. Yamada, R. Kulsrud, and H. Ji, Rev. Mod. Phys. **82**, 603 (2010).
[4]D. A. Uzdensky, B. Cerutti, and M. C. Begelman, Astrophys. J. Lett. **737**, L40 (2011).
[5]H. Ji and W. Daughton, Phys. Plasmas **18**, 111207 (2011).
[6]M. Yamada, Prog. Theor. Phys. Suppl. **195**, 167 (2012).
[7]S. Krucker, H. S. Hudson, L. Glesener, S. M. White, S. Masuda, J.-P. Wuelser, and R. P. Lin, Astrophys. J. **714**, 1108 (2010).
[8]T. D. Phan, L. M. Kistler, B. Klecker, G. Haerendel, G. Paschmann, B. U. Ö. Sonnerup, W. Baumjohann, M. B. Bavassano-Cattaneo, C. W. Carlson, A. M. DiLellis *et al.*, Nature **404**, 848 (2000).
[9]J. R. Wygant, C. A. Cattell, R. Lysak, Y. Song, J. Dombeck, J. McFadden, F. S. Mozer, C. W. Carlson, G. Parks, E. A. Lucek *et al.*, J. Geophys. Res. **110**(A9), doi:10.1029/2004JA010708 (2005).
[10]E. N. Parker, J. Geophys. Res. **62**, 509, doi:10.1029/JZ062i004p00509 (1957).
[11]E. Priest and T. Forbes, *Magnetic Reconnection - MHD Theory and Applications* (Cambridge University Press, New York, 2000).
[12]J. Birn and M. Hesse, Ann. Geophys. **23**, 3365 (2005).
[13]J. Eastwood, T. Phan, J. Drake, M. Shay, A. Borg, B. Lavraud, and M. Taylor, Phys. Rev. Lett. **110**, 225001 (2013).

[14]M. Shay, J. Drake, J. Eastwood, and T. Phan, Phys. Rev. Lett. **107**, 065001 (2011).
[15]B. U. Ö. Sonnerup, *Magnetic Field Reconnection* (North-Holland Publishing Co., Amsterdam, Netherlands, 1979), Vol. 3.
[16]J. Drake, M. Swisdak, T. Phan, P. Cassak, M. Shay, S. Lepri, R. Lin, E. Quataert, and T. Zurbuchen, J. Geophys. Res. **114**, A05111, doi:10.1029/2008JA013701 (2009).
[17]J. Birn, J. F. Drake, M. A. Shay, B. N. Rogers, R. E. Denton, M. Hesse, M. Kuznetsova, Z. W. Ma, A. Bhattacharjee, A. Otto *et al.*, J. Geophys. Res. **106**, 3715, doi:10.1029/1999JA900449 (2001).
[18]J. Yoo, M. Yamada, H. Ji, and C. E. Myers, Phys. Rev. Lett. **110**, 215007 (2013).
[19]A. Fujisawa, H. Ji, K. Yamagishi, S. Shinohara, H. Toyama, and K. Miyamoto, Nucl. Fusion **31**, 1443 (1991).
[20]E. Scime, S. Hokin, N. Mattor, and C. Watts, Phys. Rev. Lett. **68**, 2165 (1992).
[21]G. Fiksel, A. F. Almagri, B. E. Chapman, V. V. Mirnov, Y. Ren, J. S. Sarff, and P. W. Terry, Phys. Rev. Lett. **103**, 145002 (2009).
[22]Y. Ono, M. Yamada, T. Akao, T. Tajima, and R. Matsumoto, Phys. Rev. Lett. **76**, 3328 (1996).
[23]M. R. Brown, C. D. Cothran, M. Landreman, D. Schlossberg, W. H. Matthaeus, G. Qin, V. S. Lukin, and T. Gray, Phys. Plasmas **9**, 2077 (2002).
[24]S. C. Hsu, G. Fiksel, T. A. Carter, H. Ji, R. M. Kulsrud, and M. Yamada, Phys. Rev. Lett. **84**, 3859 (2000).
[25]A. Stark, W. Fox, J. Egedal, O. Grulke, and T. Klinger, Phys. Rev. Lett. **95**, 235005 (2005).
[26]H. Ji, S. Terry, M. Yamada, R. Kulsrud, A. Kuritsyn, and Y. Ren, Phys. Rev. Lett. **92**, 115001 (2004).
[27]J. Yoo, M. Yamada, H. Ji, J. Jara-Almonte, and C. E. Myers, Phys. Plasmas **21**, 055706 (2014).
[28]M. A. Shay, J. F. Drake, R. E. Denton, and D. Biskamp, J. Geophys. Res. **103**, 9165, doi:10.1029/97JA03528 (1998).
[29]M. Hesse, K. Schindler, J. Birn, and M. Kuznetsova, Phys. Plasmas **6**, 1781 (1999).
[30]H. Karimabadi, W. Daughton, and J. Scudder, Geophys. Res. Lett. **34**, L13104, doi:10.1029/2007GL030306 (2007).
[31]P. L. Pritchett, J. Geophys. Res. **115**, A10208, doi:10.1029/2010JA015371 (2010).
[32]M. Yamada, J. Yoo, J. Jara-Almonte, H. Ji, R. M. Kulsrud, and C. E. Myers, Nat. Commun. **5**, 4474 (2014).
[33]J. Birn, K. Galsgaard, M. Hesse, M. Hoshino, J. Huba, G. Lapenta, P. L. Pritchett, K. Schindler, L. Yin, J. Bchner *et al.*, Geophys. Res. Lett. **32**, L06105, doi:10.1029/2004GL022058 (2005).
[34]S. Zaharia and J. Birn, Phys. Plasmas **14**, 072101 (2007).
[35]J. Birn and M. Hesse, Phys. Plasmas **17**, 012109 (2010).
[36]J. Egedal, A. Le, and W. Daughton, Phys. Plasmas **20**, 061201 (2013).
[37]A. Le, J. Egedal, W. Daughton, V. Roytershteyn, H. Karimabadi, and C. Forest, J. Plasma Phys. **81**, 305810108 (2015).
[38]M. A. Shay, C. C. Haggerty, T. D. Phan, J. F. Drake, P. A. Cassak, P. Wu, M. Oieroset, M. Swisdak, and K. Malakit, Phys. Plasmas **21**, 122902 (2014).
[39]T. D. Phan, M. A. Shay, J. T. Gosling, M. Fujimoto, J. F. Drake, G. Paschmann, M. Oieroset, J. P. Eastwood, and V. Angelopoulos, Geophys. Res. Lett. **40**, 4475, doi:10.1002/grl.50917 (2013).
[40]K. J. Bowers, B. J. Albright, L. Yin, B. Bergen, and T. J. T. Kwan, Phys. Plasmas **15**, 055703 (2008).
[41]S. Dorfman, W. Daughton, V. Roytershteyn, H. Ji, Y. Ren, and M. Yamada, Phys. Plasmas **15**, 102107 (2008).
[42]W. Daughton, J. Scudder, and H. Karimabadi, Phys. Plasmas **13**, 072101 (2006).
[43]M. Yamada, H. Ji, S. Hsu, T. Carter, R. Kulsrud, N. Bretz, F. Jobes, Y. Ono, and F. Perkins, Phys. Plasmas **4**, 1936 (1997).
[44]G. Fiksel, D. J. D. Hartog, and P. W. Fontana, Rev. Sci. Instrum. **69**, 2024 (1998).
[45]P. Pritchett, J. Geophys. Res. **106**, 3783, doi:10.1029/1999JA001006 (2001).
[46]H. Ji, Y. Ren, M. Yamada, S. Dorfman, W. Daughton, and S. P. Gerhardt, Geophys. Res. Lett. **35**, L13106, doi:10.1029/2008GL034538 (2008).
[47]Y. Ren, M. Yamada, S. Gerhardt, H. Ji, R. Kulsrud, and A. Kuritsyn, Phys. Rev. Lett. **95**, 055003 (2005).
[48]M. Yamada, Y. Ren, H. Ji, J. Breslau, S. Gerhardt, R. Kulsrud, and A. Kuritsyn, Phys. Plasmas **13**, 052119 (2006).
[49]Y. Ren, M. Yamada, H. Ji, S. P. Gerhardt, and R. Kulsrud, Phys. Rev. Lett. **101**, 085003 (2008).
[50]T. Takizuka and H. Abe, J. Comput. Phys. **25**, 205 (1977).
[51]S. I. Braginskii, *Reviews of Plasma Physics* (Consultants Bureau, New York, 1965), Vol. 1, pp. 205–311.
[52]A. Le, J. Egedal, O. Ohia, W. Daughton, H. Karimabadi, and V. S. Lukin, Phys. Rev. Lett. **110**, 135004 (2013).
[53]W. Daughton, V. Roytershteyn, H. Karimabadi, L. Yin, B. J. Albright, S. P. Gary, and K. J. Bowers, AIP Conf. Proc. **1320**, 144 (2011).
[54]W. Daughton, V. Roytershteyn, H. Karimabadi, L. Yin, B. J. Albright, B. Bergen, and K. J. Bowers, Nat. Phys. **7**, 539 (2011).
[55]W. Daughton, T. K. M. Nakamura, H. Karimabadi, V. Roytershteyn, and B. Loring, Phys. Plasmas **21**, 052307 (2014).